Journal of Controlled Release 322 (2020) 426–438

Contents lists available at ScienceDirect

Journal of Controlled Release

journal homepage: www.elsevier.com/locate/jconrel

Opening of endothelial cell–cell contacts due to sonoporation

Inés Beekers[a,*], Merel Vegter[a], Kirby R. Lattwein[a], Frits Mastik[a], Robert Beurskens[a], Antonius F.W. van der Steen[a,b], Nico de Jong[a,b], Martin D. Verweij[a,b], Klazina Kooiman[a]

[a] Department of Biomedical Engineering, Thoraxcenter, Erasmus University Medical Center, Office Ee2302, P.O. Box 2040, 3000, CA, Rotterdam, The Netherlands
[b] Laboratory of Medical Imaging, Department of Imaging Physics, Delft University of Technology, Building 22, Room D218, Lorentzweg 1, 2628 CJ Delft, The Netherlands

ARTICLE INFO

Keywords:
Drug delivery
Microbubbles
Ultrasound
Sonoporation
Cell-cell contact opening
High-speed imaging

ABSTRACT

Ultrasound insonification of microbubbles can locally increase vascular permeability to enhance drug delivery. To control and optimize the therapeutic potential, we need to better understand the underlying biological mechanisms of the drug delivery pathways. The aim of this *in vitro* study was to elucidate the microbubble-endothelial cell interaction using the Brandaris 128 ultra-high-speed camera (up to 25 Mfps) coupled to a custom-built Nikon confocal microscope, to visualize both microbubble oscillation and the cellular response. Sonoporation and opening of cell-cell contacts by single $\alpha_V\beta_3$-targeted microbubbles (n = 152) was monitored up to 4 min after ultrasound insonification (2 MHz, 100–400 kPa, 10 cycles). Sonoporation occurred when microbubble excursion amplitudes exceeded 0.7 μm. Quantification of the influx of the fluorescent model drug propidium iodide upon sonoporation showed that the size of the created pore increased for larger microbubble excursion amplitudes. Microbubble-mediated opening of cell-cell contacts occurred as a cellular response upon sonoporation and did not correlate with the microbubble excursion amplitude itself. The initial integrity of the cell-cell contacts affected the susceptibly to drug delivery, since cell-cell contacts opened more often when cells were only partially attached to their neighbors (48%) than when fully attached (14%). The drug delivery outcomes were independent of nonlinear microbubble behavior, microbubble location, and cell size. In conclusion, by studying the microbubble–cell interaction at nanosecond and nanometer resolution the relationship between drug delivery pathways and their underlying mechanisms was further unraveled. These novel insights will aid the development of safe and efficient microbubble-mediated drug delivery.

1. Introduction

Life-threatening diseased tissue often lies beyond the vasculature. This means that intravenously administered drugs need to extravasate from the vasculature to reach their intracellular and extravascular targets. The endothelial cells that line the vessel wall are barriers that severely limit local and effective drug delivery necessary for successful treatment. To overcome the challenges these barriers present, drug delivery can be locally enhanced using lipid-coated gas microbubbles (1–10 μm) in combination with ultrasound [1,2]. These microbubbles are widely used in the clinic to improve contrast in diagnostic ultrasound imaging. When ultrasound is applied, microbubbles will oscillate, which can permeabilize cell membranes (sonoporation), open cell-cell contacts, and stimulate endocytosis [1–3]. However, the underlying physical and biological mechanisms of the microbubble–cell interaction need to be elucidated. If we can control and predict the different drug delivery pathways, microbubble-mediated drug delivery can be tuned to the requirements of a therapeutic application.

To unravel the underlying mechanisms of the microbubble–cell interaction, one needs to know which microbubble behavior is responsible for which cellular response. Therefore, we need to image both the microbubble oscillation at nanosecond temporal resolution and the ensuing detailed cellular response at nanometer spatial resolution. Until now, concurrent visualization of microbubble oscillation and endothelial cell response has only been possible using an ultra-high-speed camera coupled to a widefield microscope [4–7]. In these studies, focusing on sonoporation, the microbubble behavior was known but the cellular response was imaged at low resolution and sensitivity. Helfield et al. [4] performed an additional experiment in which they only used confocal microscopy to show sonoporation and opening of cell-cell contacts in a single example. Confocal microscopy has also been used by others to visualize the cellular response at high spatial resolution

* Corresponding author at: Office Ee2302, P.O. Box 2040, 3000 CA Rotterdam, The Netherlands.
E-mail addresses: d.beekers@erasmusmc.nl (I. Beekers), k.lattwein@erasmusmc.nl (K.R. Lattwein), f.mastik@erasmusmc.nl (F. Mastik), r.beurskens@erasmusmc.nl (R. Beurskens), a.vandersteen@erasmusmc.nl (A.F.W. van der Steen), n.dejong@erasmusmc.nl (N. de Jong), m.d.verweij@tudelft.nl (M.D. Verweij), k.kooiman@erasmusmc.nl (K. Kooiman).

https://doi.org/10.1016/j.jconrel.2020.03.038
Received 23 January 2020; Received in revised form 24 March 2020; Accepted 25 March 2020
Available online 01 April 2020

and detector sensitivity. They investigated sonoporation [8–12], membrane perforation and recovery dynamics [8], endocytosis [9], sonoprinting [10,13], lipoplex delivery [11], and cytoskeleton reorganization [12]. However, the studies using confocal microscopy lacked information on the microbubble oscillation behavior that was responsible for the cellular effect. Since single microbubble response to ultrasound is variable [14,15] even for known acoustic pressures, the underlying mechanisms of the microbubble–cell interaction could not be fully resolved.

Sonoporation has been investigated *in vitro* and in real-time, demonstrating the capability of an oscillating microbubble to create a pore in the endothelial cell membrane [4,6,7,16,17]. The transient behavior of pore formation and recovery dynamics have been studied with live cell microscopy [8,18]. Reversible sonoporation can temporarily enhance intracellular drug delivery without cell death. However, when cell membrane integrity is not restored after pore formation, sonoporation is irreversible and will eventually lead to cell death. Pore resealing times from a few seconds up to 120 s have been reported [8,16,17,19]. Fan et al. [18] showed that upon sonoporation, the amount of fluorescent marker propidium iodide (PI) uptake can be related to the size of the pore and its resealing time. This has been used to quantify the pore dynamics of kidney [18] and endothelial cells [16,20]. Nevertheless, it remained unknown how microbubble oscillation behavior correlates with the severity of sonoporation, in terms of the pore size and its resealing characteristics. When the microbubble excursion amplitude required for sonoporation was investigated, the cellular response could only be studied at low sensitivity and spatial resolution using widefield microscopy [4,7].

Opening of cell-cell contacts has been previously observed using live cell microscopy within minutes after ultrasound insonification of a non-targeted microbubble for a single example [4]. The opened cell-cell contacts remained open for tens of minutes, suggesting a prolonged enhanced drug delivery effect of this pathway. In addition, extravasation of drug compounds from the vasculature has been shown, for instance to overcome the blood-brain barrier [21,22]. It is hypothesized that this cellular response of opening the intercellular junctions is caused by the shear stress from the oscillating microbubbles, the microbubble forces on the cytoskeleton of the cell, and/or the changes in cell morphology due to sonoporation [23]. However, there is still a lack of understanding on how microbubble oscillation behavior causes the opening of cell-cell contacts and whether this is an independent drug delivery pathway or induced upon sonoporation [23].

In this study we aimed to elucidate the missing link between microbubble oscillation behavior and the occurrence of sonoporation and opening of cell-cell contacts in cultured endothelial cells. Microbubbles were targeted to the integrin $\alpha_v\beta_3$ (alpha-v-beta-3), also known as CD51/61, expressed by endothelial cells during angiogenesis [24], which is clinically relevant for cancer and atherosclerosis therapy. Ultrasound at a 2 MHz frequency was applied, commonly used in transthoracic ultrasound [25]. A unique optical imaging system was used consisting of the Brandaris 128 ultra-high-speed camera, to record the microbubble oscillation, coupled to a custom-built Nikon A1R+ confocal microscope, to visualize the cellular response. The cellular response upon insonification of a single targeted microbubble was studied by monitoring uptake of the model drug PI and by assessing opening of cell-cell contacts between adjacent cells. As a result, the microbubble–cell interaction was studied at both nanosecond and nanometer resolution (17 Mfps and 200 nm, respectively).

2. Material and methods

2.1. Endothelial cell culture

Primary human umbilical vein endothelial cells (HUVECs) from pooled donors (C2519A, LOT 437550, Lonza, Verviers, Belgium) were cultured in MV2 medium (C22121, PromoCell, Heidelberg, Germany), supplemented with 1% Penicillin-Streptomycin (15140122, Gibco, Thermo Fisher Scientific, Waltham, MA, USA). The HUVECs were grown (at 37 °C and 5% CO_2) in a humidified incubator to full confluency in T75 flasks. Next, they were detached using Accutase solution (A6964, Sigma-Aldrich, St. Louis, MO, USA) and replated on the bottom membrane of a CLINIcell (CLINIcell25–50-T, REF 00106, MABIO, Tourcoing, France) in 12 ml MV2. The CLINIcell is an acoustic compatible cell culture chamber with two gas permeable parallel membranes (thickness 50 μm, surface area 25 cm^2) [26]. The CLINIcells were incubated (at 37 °C and 5% CO_2) for two days to achieve a fully confluent cell monolayer. The HUVECs used in the experiments were between passage numbers 4 and 6.

2.2. Targeted microbubble preparation

Lipid-coated microbubbles with a C_4F_{10} gas core were produced in-house by probe sonication for 1 min, as previously described [27–29]. The coating consisted of 1,2-distearoyl-sn-glycero-3-phosphocholine (DSPC; 84.8 mol%; P6517, Sigma-Aldrich), polyoxyethylene-40-stearate (PEG-40 stearate; 8.2 mol%; P3440, Sigma-Aldrich), 1,2-distearoyl-sn-glycero-3-phosphoethanolamine-N-[carboxy(polyethylene glycol)-2000] (DSPE-PEG(2000); 5.9 mol%; 880125P, Avanti Polar Lipids, Alabaster, AL, USA), and 1,2-distearoyl-sn-glycero-3-phosphoethanolamine- N-[biotinyl(polyethylene glycol)-2000] (DSPE-PEG(2000)-biotin; 1.1 mol%; 880129C, Avanti Polar Lipids). Finally, to fluorescently label the microbubble coating, the lipid dye DiD (1,1′-dioctadecyl-3,3,3′,3′-tetramethylindodicarbocyanine perchlorate; D307, Thermo Fisher Scientific) was added before sonication.

The microbubbles were targeted to the $\alpha_v\beta_3$ integrin using biotin-streptavidin bridging, as previously described by others [7,30–34] with the exception of the type of ligand. Briefly, after washing three times by centrifugation (400*g*, 1 min) using PBS saturated with C_4F_{10}, the microbubble concentration was determined with a Coulter Counter Multisizer 3 ($n = 3$) (20 μm aperture tube, Beckman Coulter, Mijdrecht, the Netherlands). Next, 6×10^8 microbubbles were incubated on ice for 30 min with 60 μg of streptavidin (2 mg/ml stock concentration in PBS, S4762, Sigma-Aldrich) and washed. These streptavidin-conjugated microbubbles were incubated on ice for 30 min with 6 μg of biotinylated anti-human CD51/61 antibody (304412, BioLegend, San Diego, CA, USA), followed by a final washing step.

2.3. Experimental set-up

To study the microbubble-cell interaction, a unique optical imaging system was used consisting of the Brandaris 128 ultra-high-speed camera (up to 25 million frames per second, Mfps) [35] coupled to a custom-built Nikon A1R+ confocal microscope (Fig. 1A) [36]. With this system high temporal and spatial resolutions can be achieved, required to resolve the microbubble oscillation and cellular response, as explained in more detail by Beekers et al. [36]. For simultaneous imaging and ultrasound insonification, the CLINIcell was inserted into a 37 °C water tank positioned beneath the microscope. A single element focused transducer (2.25 MHz center frequency; 76.2 mm focal length; −6 dB beam width at 2 MHz of 3 mm; V305; Panametrics-NDT, Olympus, Waltham, MA, USA) was mounted in the water tank at a 45° angle, after having been calibrated using a needle hydrophone. The ultrasound and optical foci were aligned such that the cells in the CLINIcell could be both imaged and insonified (Fig. 1A). A single 2 MHz and 10-cycle burst was generated by an arbitrary waveform generator (33220A, Agilent, Palo Alto, CA, USA). A broadband amplifier (ENI A-500, Electronics & Innovation, Rochester, NY, USA) was used to obtain peak negative pressures (PNP) of 100, 200, 250, 300, and 400 kPa at the focus.

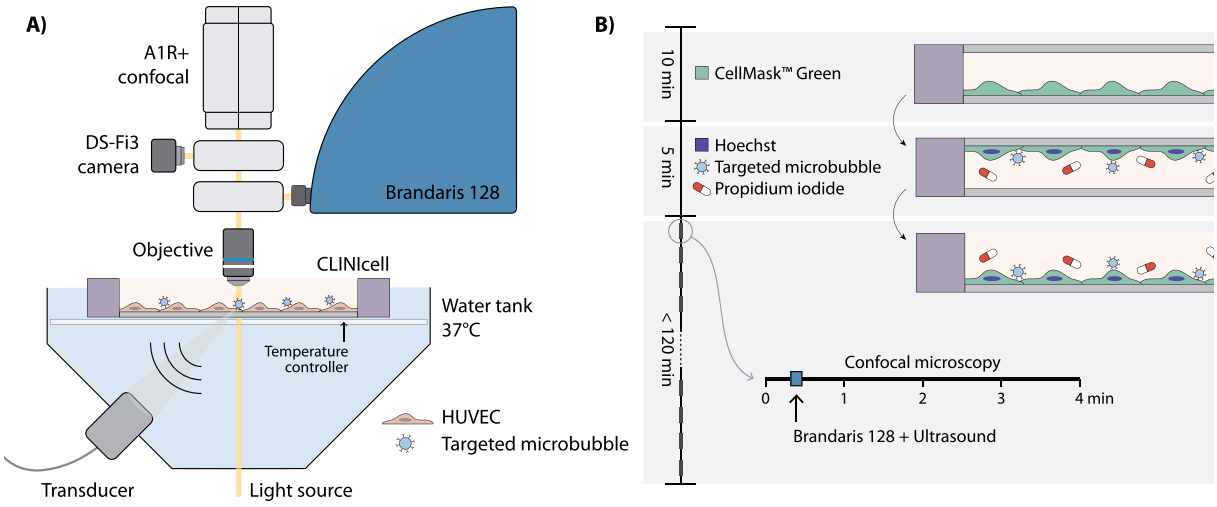

Fig. 1. Schematic representation of the experimental procedure (not drawn to scale). (A) Experimental setup to insonify a CLINIcell under a 45° angle. The optical imaging system combines an A1R+ confocal scan head (Nikon Instruments), with a DS-Fi3 colour camera (Nikon Instruments) for widefield imaging, and the Brandaris 128 ultra-high-speed camera. (B) Timeline starting with the incubation of HUVECs with fluorescent dyes and targeted microbubbles, followed by time-lapse imaging with the combined optical imaging system.

2.4. Experimental protocol

The HUVECs were stained with fluorescent dyes for live confocal microscopy imaging (Fig. 1B). They were incubated with CellMask™ Green Plasma Membrane Stain (4 μg/ml final concentration; C37608; Thermo Fisher Scientific) for 10 min inside the cell incubator to stain the cell membranes. Next, Hoechst 33342 (5 μg/ml final concentration; H3570, Thermo Fisher Scientific) was added to stain the cell nuclei and PI (25 μg/ml final concentration; P4864, Sigma-Aldrich) was added as a marker for sonoporation. The cell membrane of viable cells is impermeable for PI. When the cell membrane is compromised, PI enters the cell, binds to DNA and RNA, and becomes fluorescent [37]. Therefore, PI is often used as a marker for sonoporation to evaluate membrane perforation [4,6,18,38,39]. Additionally, CD51/61 targeted microbubbles (2×10^5 microbubbles/ml final concentration) were added and the CLINIcell was incubated during 5 min inside the cell incubator, while turned upside down to allow the targeted microbubbles to float towards the cells to achieve binding (Fig. 1B). The CLINIcell was then turned upright again such that only bound targeted microbubbles remained in the focal plane of the cells. Finally, the top membrane without cells was cut from the CLINIcell, making it feasible to image with an objective with a working distance smaller than the 5 mm spacing between the CLINIcell membranes. The same incubation timeline was used for control CLINIcells without microbubbles.

To monitor the cellular response with confocal microscopy, imaging was performed with the following four channels: (1) Hoechst excited at 405 nm, detected at 450/50 nm (center wavelength/bandwidth), (2) CellMask Green excited at 488 nm, detected at 525/50 nm, (3) PI excited at 561 nm, detected at 595/50 nm, and (4) DiD excited at 640 nm, detected at 700/70 nm. Channel 1 and 4 were excited and detected simultaneously because there is no spectral overlap between Hoechst and DiD.

Using a 100× water dipping objective (CFI Plan 100XC W, 2.5 mm working distance, Nikon Instruments), a field of view (FOV) of 74.2 × 74.2 μm (256 × 256 pixels) was scanned at 0.65 frames per second (fps). At each location, time-lapse imaging was performed for 4 min in total (Fig. 1B). This 100× objective has a high numerical aperture of 1.10; therefore, we achieve a lateral resolution up to 200 nm and an axial resolution up to 600 nm [40]. To visualize the initial cellular state, confocal microscopy time-lapse imaging started before ultrasound. Within the first minute, the light path was automatically switched from the confocal scanning head to the Brandaris 128 ultra-high-speed camera. The microbubble oscillation was then recorded at approximately 17 Mfps during ultrasound insonification. Once this recording was completed, the light path was switched back towards the confocal scanning head to visualize the cellular response. Since insonification occurred within the first minute, the cellular response upon microbubble vibration was monitored for at least 3 min (Fig. 1B).

The area to be imaged was chosen based on the following inclusion criteria: (i) the FOV showed fully confluent cells, such that there were no empty spaces in which an extra cell could have grown and all cells were at least partially attached to neighboring cells; (ii) there was a single targeted microbubble in the FOV; (iii) this targeted microbubble was located on a cell that was completely in the FOV; (iv) this cell had a single nucleus; and (v) this nucleus did not overlap with that of any neighboring cells. Per CLINIcell, a maximum of 15 locations uniformly distributed and spaced by at least 1 cm to avoid overlapping insonification were imaged within 120 min. Additional CLINIcells were used for two types of control experiments: (i) sham, i.e. without microbubbles or ultrasound; and (ii) ultrasound only, i.e. without microbubbles.

2.5. Analysis of microbubble oscillation

Microbubble oscillation recorded by the Brandaris 128 ultra-high-speed camera was quantified using custom-designed image analysis software to determine the change in radius as a function of time [41]. The initial radius (R_0) was determined from the first 10 frames without ultrasound. Microbubble excursion amplitude was defined as the difference between the maximum radius (R_{max}) and R_0. The excursion amplitude threshold for sonoporation was determined by linear discriminant analysis and defined as the average over the full microbubble size range [4].

Nonlinear microbubble behavior was studied by assessing the harmonic response. To do so, the frequency spectrum of the radius-time curve was determined using a Fast Fourier Transformation (FFT). Amplitudes were determined within a ± 300 kHz bandwidth centered at the subharmonic (1 MHz) and second harmonic (4 MHz) frequencies. The noise levels were defined as the mean amplitude within those bandwidths from the FFT of the radius-time curve before and after oscillation. When the maximum amplitude of the FFT from the radius-time curve during oscillation was at least 6 dB above the mean noise level of all recordings, a microbubble was classified as responsive

[42,43].

Finally, the asymmetry of microbubble oscillation was investigated. This was quantified by the amount of expansion (E) relative to the amount of compression (C). As previously done by others [27,43–46], the E/C ratio was defined as $E/C = (R_{max} - R_0) / (R_0 - R_{min})$. Compression-only behavior is defined by an $E/C < 0.5$, symmetric oscillation ranges from $0.5 \leq E/C \leq 2$, and expansion-only behavior as an $E/C > 2$.

2.6. Analysis of confocal time-lapse images

The image analysis aimed at studying the microbubble-mediated drug delivery pathways induced in the "cell of interest", i.e. the cell with a single bound targeted microbubble, which from now on will be referred to as *the cell*. From the time-lapse confocal microscopy before insonification, the cell was classified based on the initial state of its contact with adjacent cells. When the cell edge was fully adjacent to the neighboring cells, it was classified as having *full junctions*, and when partially adjacent it was classified as having *partial junctions*. For the controls without ultrasound, the initial cell state was determined from the first 30 s of time-lapse confocal microscopy. After ultrasound, the cellular response was evaluated by studying two different drug delivery pathways. Sonoporation was assessed based on PI uptake within the cell as described in detail below. Opening of cell-cell contacts was assessed by changes in the cell border integrity to adjacent cells based on CellMask. When a gap, or gaps, formed between the cell and its neighbor(s), the cell was classified as *retracting*. Manual classification was performed by two individual users (M.V. and I.B.) for alternating ultrasound settings and experiment days.

To determine the surface area of the cell and the microbubble location, the cell was delineated and the microbubble location was registered. The delineation and registration were performed manually using a custom-built MATLAB (The Mathworks Inc., Natick, MA, USA) routine. After cell delineation, another MATLAB routine was used to automatically segment the corresponding nucleus based on the Hoechst images. The microbubble location was quantified as the distance from the microbubble to the closest cell edge or, alternatively, to the center of the nucleus. The 4 min confocal microscopy time-lapse recording was split between before and after insonification by finding the period of time when the light path was switched towards the Brandaris 128 camera. The resulting sudden loss of CellMask signal in the confocal time-lapse recording was automatically detected using MATLAB. The first confocal frame after ultrasound was defined as $t = 0$.

During time-lapse imaging slight vertical displacements of the CLINIcell can occur within the water tank, caused by, for instance, thermal expansion of the heating element. These small displacements changed the imaging plane, and although the cell was still in the FOV, the focus drift could alter the detected fluorescent intensity. Therefore, the PI intensity in a sonoporated cell can appear to fluctuate. To correct for PI intensity variations caused by focus drift, the CellMask fluorescent intensity was used as a reference. Although CellMask stains the membrane while PI is present in the cytoplasm, it is a valid reference since endothelial cells are very thin, with a mean height of 0.9 μm at the periphery and up to 1.6 μm at the nucleus [47]. Hence, when the membrane is in focus, the cytoplasm is also within the same focal plane (600 nm). For each confocal time-lapse recording, a correction factor was determined as the ratio between the time-dependent CellMask signal and its initial value, both within the delineated cell. Next, the PI intensity detected upon sonoporation was corrected by this correction factor.

2.7. Analysis of PI uptake profiles

Upon sonoporation, the size of the pore created in the cellular membrane is closely related to the amount of PI uptake. Fan et al. [18] mathematically described this by

$$F(t) = \frac{\alpha\pi DC_0 r_0}{\beta}(1 - e^{-\beta t}) \quad (1)$$

The amount of fluorescent intensity $F(t)$ detected in a cell as a function of time is related to the initial pore radius (r_0), for a known diffusion coefficient of the PI fluorescent molecule (D), extracellular PI concentration (C_0), and imaging system dependent calibration coefficient (α). The pore size coefficient ($\alpha\pi DC_0 r_0$) is a measure for the initial pore size, defined by the initial slope of the PI uptake profile and independent of cell size. The stabilization of the fluorescent intensity is quantified by the pore resealing coefficient (β). Since PI molecules bind to both RNA and DNA in the cell cytoplasm and nucleus [37], we were interested in the amount of PI fluorescence within the delineated cell area. The fluorescent intensity $F(t)$ was defined as the sum over the pixels within the cell area after ultrasound minus the mean before ultrasound. Thereby, we corrected for any initial background noise signal (the mean 12-bit pixel intensity, ranging from 0 to 4095, before ultrasound was 150 and increased by an order of magnitude upon sonoporation).

Since the light path towards the confocal microscope was temporarily intercepted during insonification, PI uptake could already have started before $t = 0$, i.e. before the confocal light path was restored. In other words, $F(0)$ might not be zero. Therefore, Eq. (1) was adapted such that PI uptake started at $t = t_0$ and $F(t_0) = 0$. This changes Eq. (1) into

$$F(t) = \frac{\alpha\pi DC_0 r_0}{\beta}(1 - e^{-\beta(t-t_0)}) \quad (2)$$

Confocal time-lapse imaging was restored within ~2 s after ultrasound insonification, hence t_0 ranged from −2 to 0 s. The influx of PI upon pore formation was monitored as a function of time and the determined $F(t)$ was fit to Eq. (2) using a non-linear least squares approach in MATLAB to determine the pore size coefficient ($\alpha\pi DC_0 r_0$), the pore resealing coefficient (β), and the starting time of pore formation (t_0). The time t_{90} at which 90% of the asymptotic value, $F(\infty) = \alpha\pi DC_0 r_0/\beta$, was reached is

$$t_{90} = \frac{-\ln(1 - 0.9)}{\beta} + t_0 = \frac{2.30}{\beta} + t_0. \quad (3)$$

When $t_{90} < 120$ s it means PI uptake stabilizes, presumably caused by pore resealing [16]. However, in the case of high PI uptake, the detected fluorescent intensity can also stabilize due to image saturation or DNA/RNA saturation. Although more PI might be entering the cell, this increase can no longer be detected when the pixels are already saturated (i.e. when the 12-bit pixels are at their maximum value of 4095) or when there is no free DNA or RNA left for PI to bind to. In this study, the imaging settings were chosen such that high PI uptake results in image saturation before DNA/RNA saturation. The optimal settings were determined such that the pixels in the nucleus were image saturated when adding 0.1% Triton X-100 (X100, Sigma-Aldrich), which causes non-resealing membrane disruptions leading to DNA/RNA saturation. By doing so, we could easily identify when the fluorescent intensity of PI stabilized by image saturation, since pixels reached their maximum 4095 value, and we avoided the otherwise indiscernible DNA/RNA saturation. Image saturation starts in the cell nucleus, since there the fluorescent intensity is highest because there is more DNA for PI to bind to. Therefore, when 90% of the pixels in the segmented nucleus reached the 12-bit value, the cell was classified as saturated. Based on the pore resealing coefficient and signal saturation, the PI uptake curves were classified in the following three categories: (i) *resealing* < 120 *s*, i.e. when PI uptake stabilized with $t_{90} < 120$ s without saturation; (ii) *non-resealing*, i.e. when PI uptake did not stabilize within 120 s (i.e. $t_{90} > 120$ s); and (iii) *saturated*, i.e. when PI uptake stabilized with $t_{90} < 120$ s due to image saturation.

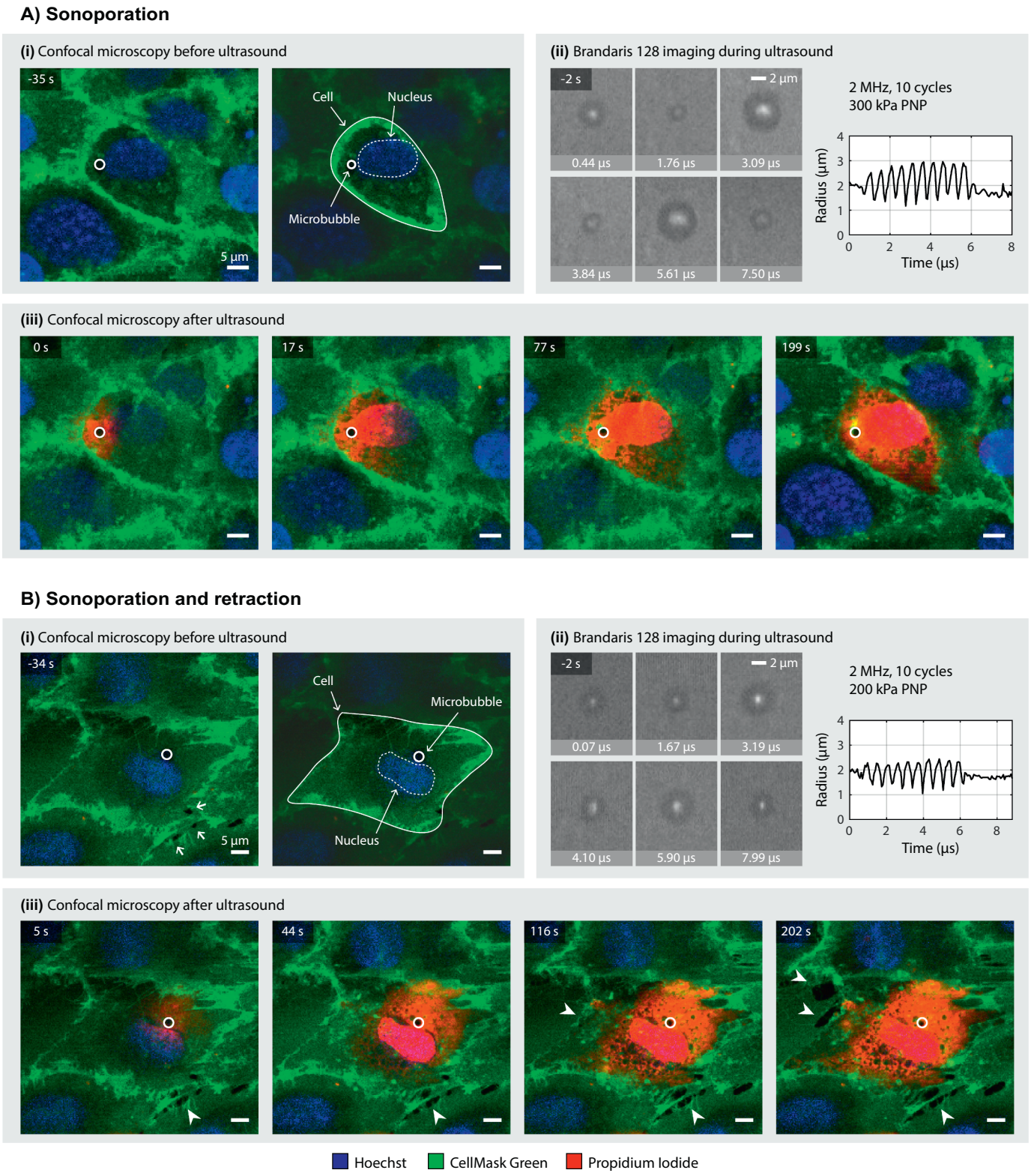

Fig. 2. Cellular response upon ultrasound insonification of a targeted microbubble imaged with combined confocal microscopy and Brandaris 128 ultra-high-speed imaging. Selected frames are shown of (i) the initial cellular state with cell delineation and segmentation, (ii) the Brandaris 128 recording with the determined microbubble radius as a function of time, and (iii) of the cellular response. (A) Sonoporation of a cell that initially had full junctions and remained intact. (B) Sonoporation and retraction of a cell that initially had partial junctions. Partial junctions are indicated by the arrows in (i), and retraction is indicated by the arrowheads in (iii).

2.8. Statistical analyses

The occurrence of a cellular pathway was presented in relative frequencies (%). This categorical data was tested for significant differences among groups using a χ^2 test. Quantitative data were assumed to be not normally distributed, and therefore presented in median and interquartile ranges and tested for significance using the Mann-Whitney *U* test. Statistically significant differences were indicated in the graphs with asterisks by using * for $p < .05$, ** for $p < .01$, and *** for $p < .001$. A Spearman's rank-order correlation was performed to determine the relationship between the microbubble excursion amplitude and the pore size coefficient. All statistical analyses were performed using MATLAB.

3. Results

3.1. Drug delivery pathways

We evaluated the cellular response of 152 cells to a single targeted microbubble upon ultrasound insonification, in 21 different CLINIcells. Additionally, the response of 44 cells was monitored without microbubbles to assess the effect of ultrasound only experiments in four CLINIcells. To control for the experimental procedure, we also evaluated the response of 32 cells during sham experiments in three CLINIcells.

Four distinct cellular responses were observed: no effect, retraction, sonoporation, or sonoporation and retraction. A typical example of a sonoporated cell is shown in Fig. 2A, where selected frames of confocal microscopy and Brandaris 128 imaging are depicted. The corresponding confocal microscopy recording is shown in Video 1. Before ultrasound, in Fig. 2A(i) a single microbubble (R_0 = 2.00 μm) was located next to the nucleus, no PI was observed in the cell, and the cell-cell contacts were fully adjacent to the neighboring cells. During ultrasound, the microbubble excursion amplitude was determined from the Brandaris 128 recording to be R_{max}-R_0 = 0.95 μm (Fig. 2A(ii)). After ultrasound, PI uptake was observed at the location of the microbubble and spread throughout the cell over time, meanwhile the cell-cell contacts remained intact (no retraction), as shown in Fig. 2A(iii). In Fig. 2B, a typical example of sonoporation and retraction induced by the oscillating microbubble is shown. The corresponding confocal microscopy recording is shown in Video 2. Before ultrasound, there was no PI observed in the cell and the single microbubble (R_0 = 1.91 μm) was located next to the nucleus (Fig. 2B(i)). The white arrows show the initial cell-cell contacts that were classified as partial junctions. During ultrasound, the microbubble excursion amplitude was R_{max}-R_0 = 0.54 μm, as shown in Fig. 2B(ii). After ultrasound (Fig. 2B(iii)), PI uptake was observed locally around the microbubble and then diffused throughout the cell. After 5 s the cell had already started to retract (white arrowheads in Fig. 2B(iii)). Retraction became more severe over the following 3 min. After 202 s, retraction was even observed on the other side of the cell, although it was fully adjacent at that location before ultrasound. In both examples, the PI intensity was brighter in the nucleus than in the cytoplasm, since there is more DNA for PI to bind to in the nucleus.

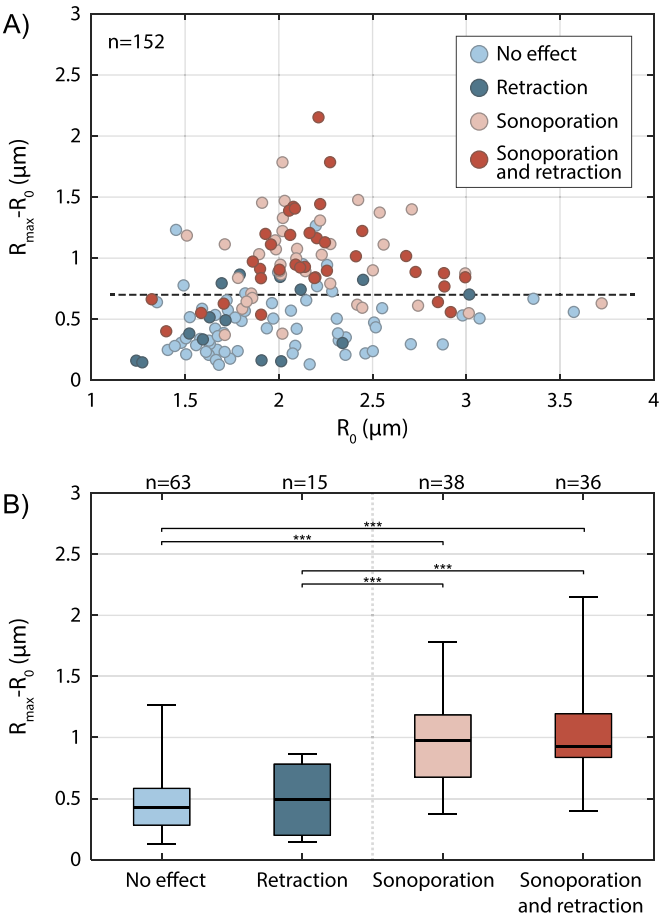

Fig. 3. Microbubble excursion amplitude (R_{max}-R_0) inducing no cellular effect (light blue), retraction (dark blue), sonoporation (pink), or both sonoporation and retraction (red). (A) R_{max}-R_0 as a function of the initial microbubble radius (R_0) for each cellular response. The dashed line indicates the 0.7 μm threshold for sonoporation. (B) Median and interquartile range of excursion amplitude for each cellular response. The whiskers range from the minimum to maximum value and statistical significance was indicated with ***$p < .001$. (For interpretation of the references to colour in this figure legend, the reader is referred to the web version of this article.)

The occurrence of the four different cellular responses is reported in Table 1. The sham and ultrasound only experiments never induced sonoporation. The vast majority (93.4%) of these cells showed no cellular effect at all, independent of acoustic pressure. Retraction was only observed in 6.6% of all cells treated without microbubbles (5 out of 76 cells for both sham and ultrasound only). When treatment consisted of ultrasound insonification of targeted microbubbles, pressure dependence was observed. At 100 kPa PNP, there was no sonoporation

Table 1
Occurrence of cellular effects for sham (i.e. control without microbubbles and ultrasound), ultrasound only, and upon treatment with ultrasound and a targeted microbubble. Values reported as percentage (%) of the total amount of cells evaluated for each setting.

Cellular response	Sham	Ultrasound only					Ultrasound and targeted microbubble				
	0 kPa	100 kPa	200 kPa	250 kPa	300 kPa	400 kPa	100 kPa	200 kPa	250 kPa	300 kPa	400 kPa
	n = 32	n = 8	n = 8	n = 9	n = 9	n = 10	n = 18	n = 43	n = 47	n = 31	n = 13
No effect (%)	93.8	100	87.5	88.9	100	90	83.3	62.8	23.4	32.3	0
Retraction (%)	6.3	0	12.5	11.1	0	10	16.7	2.3	21.3	3.2	0
Sonoporation (%)	0	0	0	0	0	0	0	27.9	10.6	41.9	61.5
Sonoporation and retraction (%)	0	0	0	0	0	0	0	7.0	44.7	22.6	38.5

induced and still only a small subgroup (3 out of 18 cells) showed retraction. However, for higher pressures the amount of sonoporated cells increased. At 400 kPa PNP, an oscillating microbubble always induced sonoporation. There was no clear correlation between retraction and acoustic pressure.

3.2. Microbubble oscillation behavior

The microbubbles studied had a mean R_0 of 2.1 μm, ranging from 1.2 μm to 3.7 μm. Insonifying these microbubbles from 100 kPa to 400 kPa PNP resulted in excursion amplitudes ranging from 0.1 μm to 2.2 μm (Fig. 3A; see Supplementary Fig. 1 for a separate excursion amplitude graph for each studied PNP). The highest excursion amplitudes were observed at R_0 of 2.2 μm and corresponded to the expected resonance size for DSPC-based microbubbles at 2 MHz [27]. All microbubbles were still targeted to the cell after insonification, and the median shrinkage (with IQR, interquartile range, between brackets) of the microbubbles was 92.1% (87.2%–97.3%), defined as the ratio between the final and initial radius. The excursion amplitudes inducing sonoporation (pink and red) were significantly larger than those where no sonoporation was induced (Fig. 3B). Using a linear discriminant analysis, the mean threshold for sonoporation was found to be R_{max}-R_0 > 0.7 μm (Fig. 3A). However, there was no distinct microbubble excursion amplitude associated with retraction. Since microbubble excursion can also be quantified by considering the minimum radius during oscillation (R_{min}) or relative to R_0, the statistical comparisons between the different cellular responses were also performed for (R_{max}-R_{min})/R_0, R_0-R_{min}, and R_{max}-R_{min}. The same statistical differences ($p < .001$) were found between sonoporated and non-sonoporated cells, and the non-significant differences between retracting and non-retracting cells remained.

To evaluate the effect of nonlinear microbubble behavior on drug delivery, we determined if microbubbles exhibited a subharmonic or second harmonic frequency response. The FFT amplitude (mean ± standard deviation) of the subharmonic noise level was 21 ± 13 nm (−18 dB below average fundamental) and that of the second harmonic noise level was 11 ± 6 nm (−23 dB below average fundamental). Only 6 out of 152 microbubbles (4%) had a subharmonic response. The presence of subharmonics did not correlate with a higher occurrence of sonoporation and/or retraction. On the other hand, 105 out of 152 microbubbles (69%) exhibited a second harmonic response, as shown in Fig. 4A. Significantly ($p < .01$) more microbubbles responded at the second harmonic frequency when sonoporation was induced (49% no effect, 67% retraction only, 84% sonoporation only, 89% sonoporation and retraction). However, the second harmonic amplitude normalized to the fundamental was not higher for microbubbles inducing sonoporation and a second harmonic response was not associated with retraction (Fig. 4A).

The asymmetry of microbubble oscillation quantified as E/C is shown in Fig. 4B. The recorded microbubbles presented with a full range of E/C ratios, from compression-only behavior ($E/C = 0.13$) to expansion-only behavior ($E/C = 2.15$). The E/C resulting in sonoporation was significantly larger than that of microbubbles that did not induce sonoporation (Fig. 4B). However, no significant differences were found in E/C for retraction.

3.3. Initial integrity of cell–cell contacts

As described in Section 2.6, the cells were classified into two subcategories based on the integrity of cell-cell contacts before ultrasound: partial junctions ($n = 88$, Fig. 2B) and full junctions ($n = 64$, Fig. 2A). The median (with IQR between brackets) excursion amplitude of microbubbles attached to a cell with partial junctions was 0.65 (0.38–0.94) μm and with full junctions 0.65 (0.42–1.05) μm. The cells in the control experiments were also classified using the same criteria.

When treated with ultrasound and microbubbles, the occurrence of

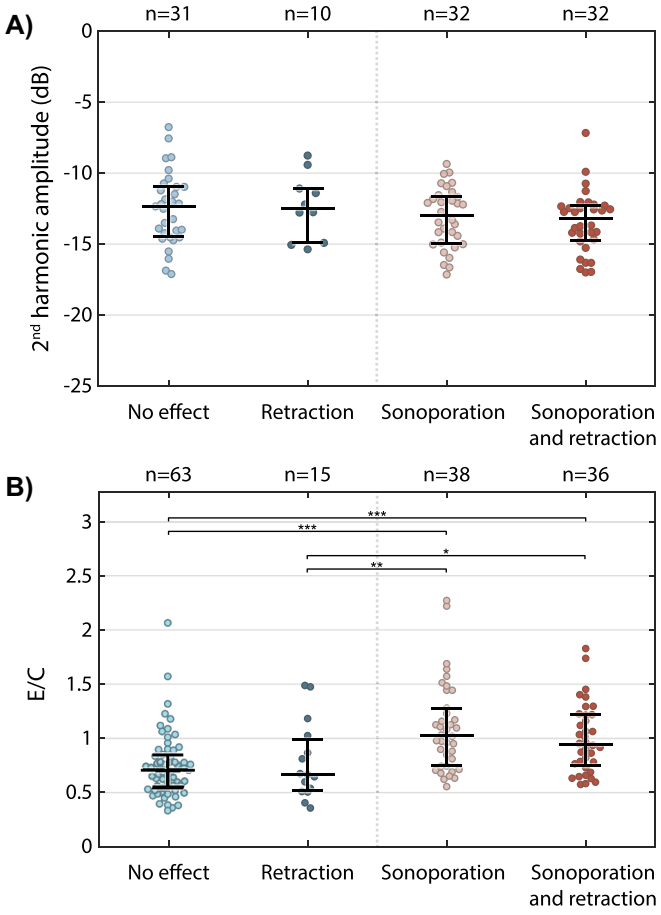

Fig. 4. Nonlinear microbubble oscillation behavior. (A) Second harmonic amplitude normalized to the fundamental for each cellular response. (B) Asymmetry of microbubble oscillation quantified as the ratio of expansion over compression (E/C) for each cellular response. The medians and interquartile ranges are overlaid. Statistical significance is indicated with *$p < .05$, **$p < .01$, and ***$p < .001$.

sonoporation was the same for both cells with partial junctions (48.9%) and with full junctions (48.4%), as shown in Fig. 5A. In the case of partial junctions, 65.1% of the sonoporated cells also retracted, while this was only 25.8% of the sonoporated cells with full junctions. For both cell junction subcategories, the sham and ultrasound only treatments never induced sonoporation. In contrast to sonoporation, retraction occurrence was affected by the initial integrity of the cell-cell contacts (Fig. 5B). After treatment with ultrasound and microbubbles, retraction occurred significantly ($p < .001$) more often when cells initially had partial junctions (47.73%) than when they had full junctions (14.1%) (Fig. 5B, US + MB). Sonoporation was only observed in 66.7% of cells with partial junctions that retracted (28 out of 42 cells), whereas almost all cells with full junctions that retracted were also sonoporated (88.9%, 8 out of 9 cells). Retraction without sonoporation in cells with partial junctions was similar for sham (13.3%), ultrasound only (13.6%), and treatment with ultrasound and microbubbles (15.91%). Retraction of cells with full junctions was never observed for the sham and ultrasound only treatments.

3.4. Cell size and microbubble location

The median (with IQR between brackets) cell area was 908 (725–1093) μm^2. There was no significant difference in cell area between the four distinct cell responses, as shown in Fig. 6A. Additionally, there was no significant difference in the location of the targeted microbubble on the cell, quantified as the distance from the microbubble

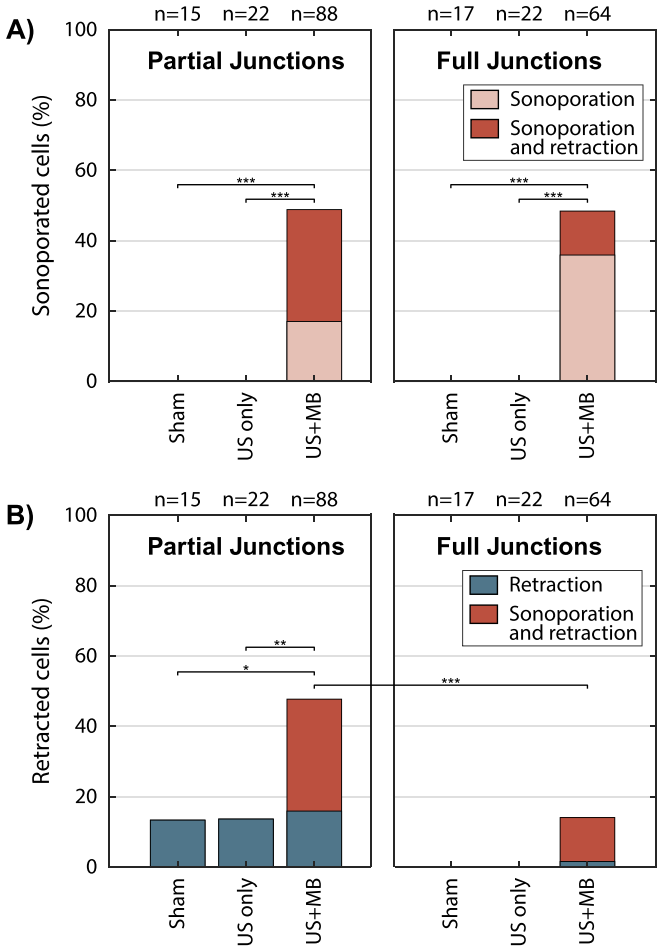

Fig. 5. The cellular response of cells with partial or full junctions, classified based on the initial integrity of cell-cell contacts. (A) Occurrence of sonoporation, with or without retraction. (B) Occurrence of retraction, with or without sonoporation. Statistical significance indicated with $*p < .05$, $**p < .01$, $***p < .001$; US = ultrasound; MB = microbubble.

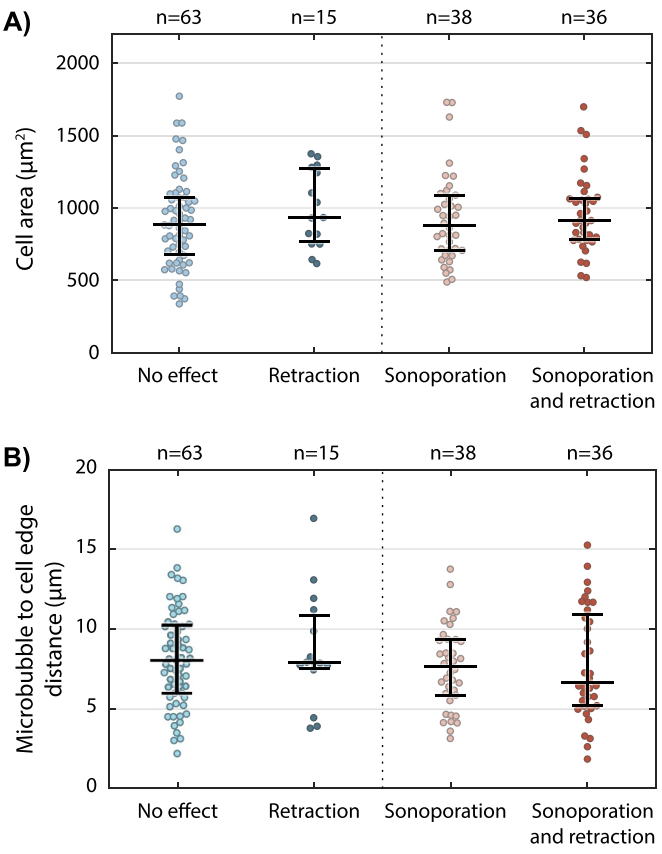

Fig. 6. Effect of (A) cell area and (B) microbubble location on the cellular response. The medians and interquartile ranges are overlaid. (For interpretation of the references to colour in this figure legend, the reader is referred to the web version of this article.)

to the closest cell edge (Fig. 6B) or, alternatively, as the distance from the microbubble to the nucleus. Cells with partial junctions had a median area of 1021 (817–1215) μm^2, and therefore were significantly ($p < .001$) larger than cells with full junctions, at 794 (621–928) μm^2. Also, the median distance of the targeted microbubble to the cell edge was significantly ($p < .001$) larger for cells with partial junctions [8.4 (6.4–11.1) μm], than for cells with full junctions [6.7 (4.7–8.5) μm]. Within these junction subcategories, there was still no significant difference in cell area or distance from the microbubble to the edge between the four cellular responses.

3.5. PI uptake profiles

Three typical examples of PI uptake profiles upon sonoporation are shown in Fig. 7. In the first example (Fig. 7A), the sonoporated cell had a PI uptake profile (Fig. 8, blue) that stabilized within 120 s, since 90% of the asymptotic value was reached after 25 s (i.e. $t_{90} = 25$ s). Signal saturation occurred in only 9.9% of the pixels in the nucleus. Therefore, this cell was classified as *resealing < 120 s*. In the second example (Fig. 7B), the PI uptake curve (Fig. 8, gray) did not stabilize within 120 s, since $t_{90} = 170$ s. Signal saturation occurred in 16% of the pixels in the nucleus. Therefore, this cell was classified as *non-resealing*. In the third example (Fig. 7C), the PI uptake curve (Fig. 8, red) stabilized within 120 s, since $t_{90} = 81$ s. However, 97% of the pixels in the nucleus were saturated, so this cell was classified as *saturated*.

The pore size coefficient ($\alpha\pi DC_0r_0$) and pore resealing coefficient (β) of all sonoporated cells are shown in Fig. 9A. The classification based on the resealing time of the pore and the signal saturation in the nucleus separates the cells into three groups. Additionally, the pore size coefficients (median and IQR between brackets) of the saturated class [0.97 (0.68–1.73) × 10^6] were significantly ($p < .001$) larger than that of the cells classified as resealing < 120 s [0.30 (0.14–0.45) × 10^6] or non-resealing [0.18 (0.11–0.25) × 10^6]. As shown in Fig. 9B, larger microbubble excursion amplitudes correlated with larger pore size coefficients upon sonoporation (Spearman correlation coefficient $\rho = 0.53$, $p < .001$). Moreover, the excursion amplitudes (median and IQR between brackets) of the saturated class [1.22 (1.03–1.45) μm] were significantly ($p < .001$) larger than that of cells classified as resealing < 120 s [0.88 (0.77–1.13) μm] or non-resealing [0.89 (0.62–1.00) μm]. The microbubble excursion amplitude did not distinguish between resealing or non-resealing pores.

4. Discussion

Sonoporation and the opening of cell-cell contacts upon ultrasound insonification of a single targeted microbubble were evaluated. Using high temporal and spatial resolution, we resolved both the microbubble oscillation and the cellular response. Susceptibility to sonoporation and opening of cell-cell contacts clearly depended on microbubble oscillation behavior and the initial state of the endothelial cell. Furthermore, quantification of sonoporation based on cellular PI uptake correlated with microbubble behavior and was used to assess reversibility of sonoporation.

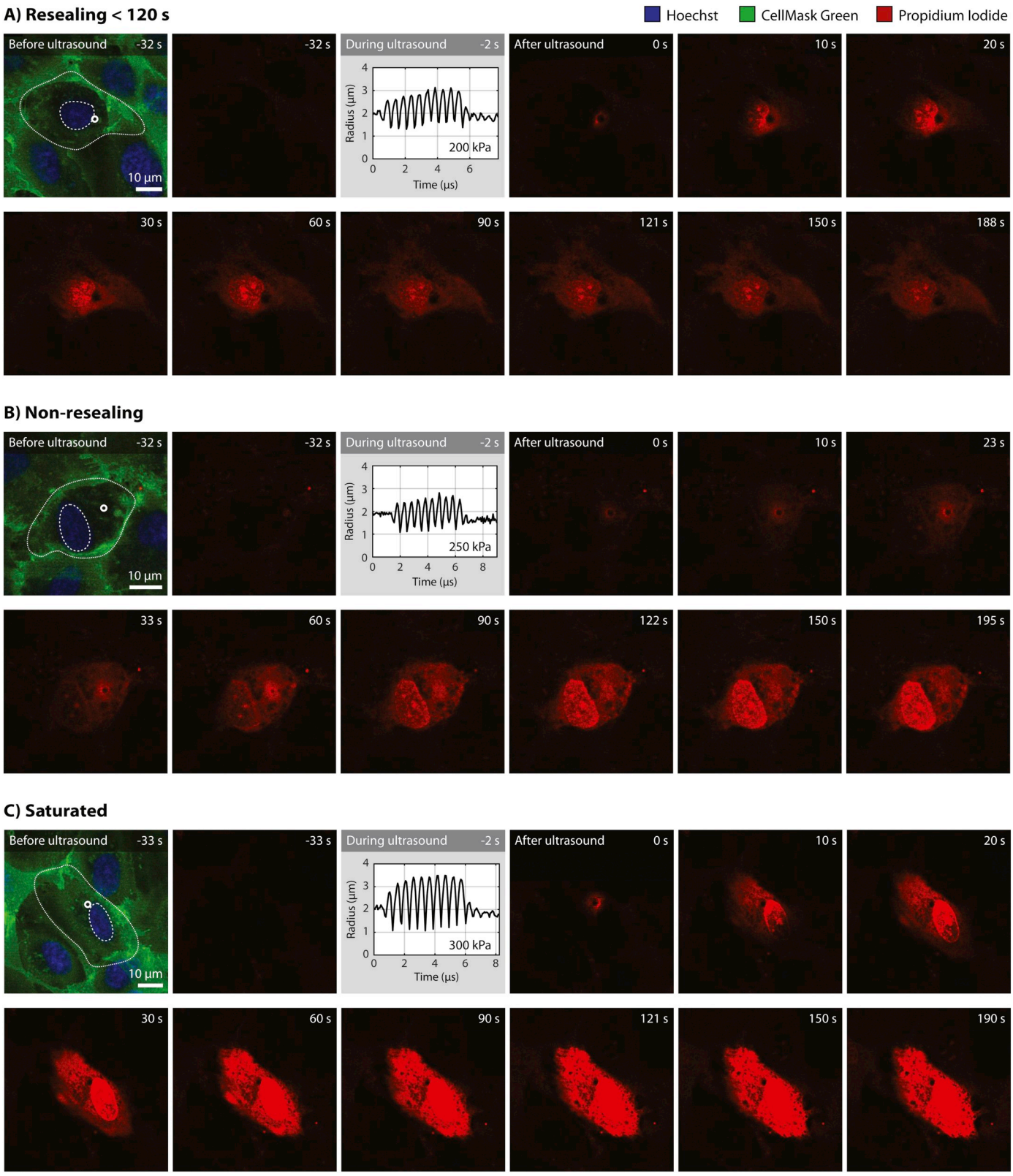

Fig. 7. Different PI uptake categories upon sonoporation imaged with confocal microscopy. The initial cellular state is shown (composite image of CellMask Green, Hoechst, and PI) with the cell delineation (solid line), nucleus segmentation (dashed line), and microbubble location (white circle). During ultrasound insonification, the change in microbubble radius is shown as a function of time. All other frames show the PI imaging channel only, before and after ultrasound. (A) PI uptake classified as resealing < 120 s. (B) PI uptake classified as non-resealing. (C) PI uptake classified as saturated. The resulting PI uptake curves of each example are shown in Fig. 8.

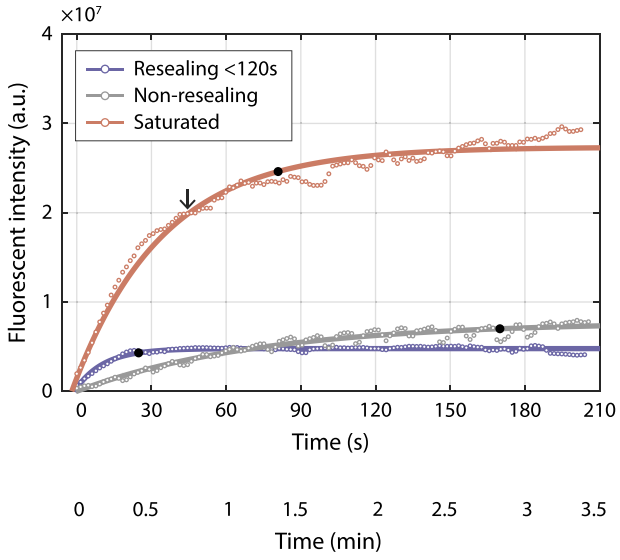

Fig. 8. Cellular PI uptake curves shown as the fluorescent intensity as a function of time ($F(t)$, circles) and the corresponding fit to the mathematical model of Eq. (2) (solid lines). The three examples correspond to those in Fig. 7 for each category: resealing < 120 s (blue, Fig. 7A), non-resealing (gray, Fig. 7B), and saturated (red, Fig. 7C). The black dots indicate the time t_{90} at which 90% of the asymptotic value was reached (Eq. (3)). The arrow marks the time at which 90% of the pixels in the nucleus were saturated; a.u. = arbitrary unit. (For interpretation of the references to colour in this figure legend, the reader is referred to the web version of this article.)

4.1. Microbubble oscillation behavior

The ultra-high-speed recordings of microbubble oscillation revealed that sonoporation correlated with large excursion amplitudes, while there was no direct relationship between microbubble excursion and the opening of cell-cell contacts (Fig. 3). Sonoporation was induced for absolute excursion amplitudes R_{max}-R_0 > 0.7 μm, similar to the previously found thresholds at 2 MHz of R_{max}-R_0 > 0.72 μm (using 16 cycles) or R_{max}-R_0 > 1.02 μm (using 8 cycles) by Helfield et al. [4]. A relative vibration threshold of 0.5 at 1 MHz (with 6× 10 cycles) was reported by Kooiman et al. [7], which corresponds to an absolute threshold of R_{max}-R_0 > 0.65 μm (for a mean R_0 of 2.2 μm and symmetric oscillation), similar to our findings.

Microbubbles that induced sonoporation exhibited a second harmonic response more often than those that did not result in sonoporation. Since nonlinear behavior increases with microbubble excursion amplitude [48], this could be inherent to the larger excursions that result in sonoporation. We found no differences in the cellular response when the second harmonic amplitude was normalized to the fundamental (Fig. 4A). The E/C ratio was also higher in the case of sonoporation (Fig. 4B) only because the expansion phase becomes more dominant with increasing acoustic pressures, and thus excursion amplitudes [49,50]. Van Wamel et al. [6] hypothesized that cells can better withstand compression than elongation forces, thereby suggesting that compression-only (E/C < 0.5) could be more effective in sonoporation. However, in this study we found that nonlinear or asymmetric microbubble behavior itself did not affect the cellular response.

The occurrence of sonoporation or opening of cell-cell contacts was found to be independent of the initial microbubble size for R_0 ranging from 1.24 to 3.72 μm, as previously found by others who studied similar size distributions [4,7]. However, to achieve high enough excursion amplitudes while insonifying at relatively low acoustic pressures, the microbubble size distribution should match the ultrasound frequency such that microbubbles are insonified at resonance. In this study, microbubbles were insonified at their mean resonance frequency of 2 MHz [27]. We limited our study to a single frequency, since Helfied et al. [4] only showed subtle differences between 0.5, 1, and 2 MHz. The excursion amplitude, i.e. acoustic pressure, plays a more important role than the frequency of oscillation, i.e. the ultrasound frequency (within the clinically relevant range 0.5 to 4 MHz). However, the microbubble–cell interaction upon insonification with longer bursts or repeated treatment remains open for investigation. For instance, when using low acoustic pressures ≤200 kPa for longer treatment duration, the stimulation of the mechanosensory channels could possibly induce different drug delivery pathways, such as stimulated endocytosis [23].

The susceptibility to sonoporation or opening of cell-cell contacts was independent of the microbubble's location on the cell (Fig. 6B). This is favorable for the clinical applicability, since *in vivo* it would be impossible to control exact microbubble location on the cell membrane. Kooiman et al. [7] also found sonoporation to be independent of microbubble location, albeit based on a manual classification of

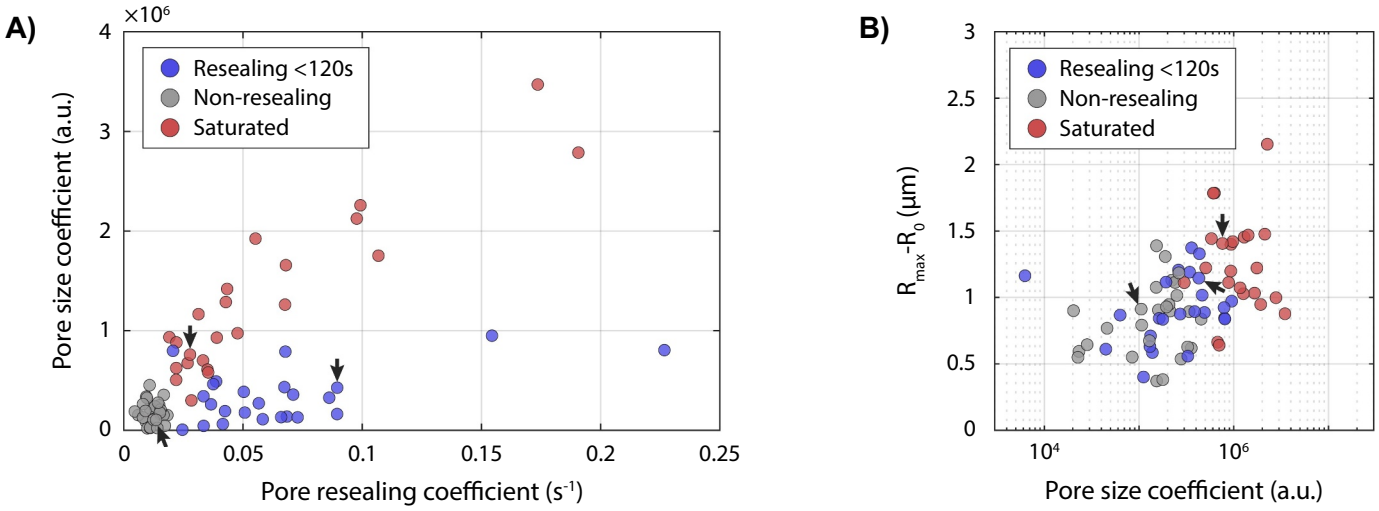

Fig. 9. Quantification of PI uptake upon sonoporation (n = 74) and the resulting classification as resealing < 120 s (blue), non-resealing (gray), and saturated (red). The arrows indicate the data points corresponding to the examples in Figs. 7 and 8. (A) The pore size coefficient as a function of the pore resealing coefficient. (B) The microbubble excursion amplitude (R_{max}-R_0) as a function of the pore size coefficient; a.u. = arbitrary unit. (For interpretation of the references to colour in this figure legend, the reader is referred to the web version of this article.)

microbubble positioning for 31 cells. Additionally, drug delivery was also independent of cell area (Fig. 6A), and thus all cell sizes seem to be equally susceptible to therapy.

4.2. Opening of cell–cell contacts due to sonoporation

Retraction of non-sonoporated cells was observed as often for both the control and ultrasound and microbubble experiments, while the enhanced retraction upon ultrasound and microbubbles only occurred upon sonoporation (Fig. 5B). From this we deduce that microbubble-mediated opening of cell-cell contacts only occurred due to sonoporation. Additionally, to open cell-cell contacts the targeted microbubble did not have to be near the cell edge (Fig. 6B), although that is often hypothesized [1,23]. Therefore, our results suggest that the opening of cell-cell contacts is a biological response triggered upon sonoporation, instead of an independent drug delivery pathway mechanically induced by microbubble oscillation. The retraction did not directly correlate to microbubble oscillation behavior (Fig. 3) and was strongly affected by the initial cell state (Fig. 5B), in contrast to the mechanical induced effect of sonoporation. This reinforces our conclusion that opening of cell-cell contacts is a cellular response mechanism and not directly caused by a microbubble mechanically rupturing the junctions. To the best of our knowledge, this is the first study that investigated the relationship between these two microbubble-mediated vascular drug delivery pathways in real-time and in the same field of view. Live cell imaging showing opening of endothelial cell-cell contacts had only been reported for a single example and without studying its correlation with sonoporation [4].

The initial cell integrity affected the susceptibility to opening of cell-cell contacts, because it occurred significantly more often when cells initially had partial junctions (Fig. 5B). About 14% of cells with partial junctions even suffered from retraction in sham and in ultrasound only experiments, independent of the acoustic pressures. This retraction without treatment could be attributed to, for example, the imaging procedure (phototoxicity), the exposure of the CLINIcell to the open air after cutting out the top membrane, or the absence of 5% CO_2. The different susceptibility to microbubble-mediated treatment between partial and full junctions could mean that under physiological conditions that result in intercellular gaps, ranging from 0.3 to 4.7 μm in tumor vasculature [51,52] or during inflammation [53,54], the drug delivery pathway of opening cell-cell contacts is induced more often. At the same time, it emphasizes the importance of a realistic model to study the opening of cell-cell contacts. In previous studies, endothelial cell confluency varied from ~70% to full confluency so not all cells were completely adjacent to their neighbors. Additionally, the integrity of the cell-cell contacts before treatment was not assessed in these previous studies [4,16,55]. The only example in literature reporting the opening of endothelial cell-cell contacts was on a not fully confluent monolayer of endothelial cells having partial junctions [4]. In our study, the initial cell integrity was assessed using a CellMask cell membrane dye. However, this dye does not specifically stain for intercellular junctions and can eventually internalize, leading to a poorer co-localization with the plasma membrane. In the current study the plasma membrane remained well stained throughout the entire 120 min. Now that we observed the importance of the initial integrity of cell-cell contacts, in future studies the integrity of intercellular junctions could be more precisely assessed using specific fluorescent dyes.

A limitation of our study is that cellular response was only monitored up to 4 min after ultrasound insonification. Within that time frame it was not possible to study the recovery of cell-cell contacts, since Helfield et al. [4] showed that cell-cell contacts can remain open for tens of minutes. For long-term effects and recovery studies, the experimental conditions would need to be further optimized to reduce spontaneous retraction. Finally, when translating to *in vivo* studies often extravasation is assessed as a measure for the opening of intercellular junctions [56,57], without monitoring sonoporation. If extravasation of a fluorescent compound would also be monitored *in vitro* using a different set-up than the CLINIcell, allowing for measurements on the basolateral side of the monolayer, both intracellular delivery by sonoporation and extravascular delivery by opening of intercellular junctions could be quantified. Additionally, since we found that retraction only occurred upon sonoporation, assessing cell membrane permeability and the possible resulting cell death *in vivo* is of great importance.

4.3. Transient pore formation

Based on cellular PI uptake upon sonoporation, the transient behavior of pore formation was quantified with the pore size and resealing coefficients, which resulted in three distinct classifications. Cells with pores that resealed within 120 s were assumed to be reversibly sonoporated, while irreversible sonoporation occurred when there was no resealing within 120 s [16]. We found that microbubble excursion amplitudes above 0.7 μm induced sonoporation, and the larger the excursion amplitude the bigger the pore that was created (Fig. 9B). This has never been observed before, since it was not possible to image both the microbubble oscillation behavior and detailed cellular response. Although intuitively there should be a higher chance for a small pore to reseal within 120 s, there was no clear correlation between pores resealing < 120 s and the pore size coefficient or microbubble excursion amplitude (Fig. 9B). Van Rooij et al. [16] also did not find a correlation between smaller pore size and resealing within 120 s. The intrinsic variability among cells seems to influence membrane resealing more than the microbubble behavior and pore size. Therefore, cellular recovery mechanisms should be further unraveled by studying the underlying resealing mechanisms.

The mathematical model described by Fan et al. [18] considers any PI uptake plateau to be caused by pore resealing. However, we observed that many of the cells that plateau within < 120 s, thus appearing to reseal, actually suffered from a saturated PI signal (Figs. 8 and 9). Saturation occurred when the pore size was largest. Reversibility of sonoporation cannot be assessed for the saturation class since the pore might remain open while the corresponding PI increase can no longer be detected. It is unclear if previous studies accounted for PI stabilization due to either image saturation or DNA/RNA saturation [16,18,20]. Therefore, it is possible that cells were assumed to be reversibly sonoporated when PI uptake plateaued due to PI saturation. Another difference with a previous study is that we monitored the PI uptake within the entire cell, while van Rooij et al. [16] determined the PI uptake profiles only within the nucleus. Therefore, small pores that quickly resealed might be missed if their PI uptake profiles started in the cytoplasm. In future sonoporation studies the limited dynamic range of an imaging system should be considered. On the one hand, when interested in low uptake, i.e. small pores that quickly reseal, PI signal saturation for the larger pores is often inevitable. On the other hand, when interested in the high uptake, i.e. larger pores that do not or slowly reseal, the imaging settings can be adjusted such that image saturation is avoided while missing the initial and lower PI changes. However, in that case the fluorescent intensity could reach an equilibrium when there is no free DNA or RNA remaining for PI to bind to. Therefore, when avoiding image saturation, one should properly account for DNA/RNA saturation.

In this study we chose to have the cells on the bottom membrane of the CLINIcell to ensure that a targeted microbubble that did not bind would float up. Since the targeted microbubble was located between the objective and the cells, the microbubble gas core caused shadowing, impeding the laser to image directly underneath it (see Fig. 7A for an example). With this orientation it was not possible to directly image the created pore. Moreover, the imaging dependent calibration coefficient α (Eqs. (1) and (2)) was not determined in this study. Nevertheless, the pore size coefficient provides us with relative sizes because all imaging

was performed under the same fluorescent imaging conditions, i.e. with the same α, and using the same extracellular PI concentration (C_0). Another limitation of this study is that reversibility could only be derived from the PI uptake profile. Literature has used two separate experiments to demonstrate the correlation between the occurrence of pore resealing within 120 s and cell viability [16]. However, if both the pore resealing timeline and cell viability were to be studied simultaneously with live cell microscopy, the underlying biological mechanisms leading to cell death could be further unraveled.

5. Conclusion

Using a state-of-the-art optical imaging system allowed for microbubble-mediated drug delivery to be studied with high sensitivity at short timescales, while also achieving the nanosecond resolution needed to resolve microbubble oscillation. Sonoporation and opening of cell-cell contacts by ultrasound insonification of targeted microbubbles were investigated. We found that larger microbubble excursion amplitudes (R_{max}-R_0 > 0.7 μm) correlated with the occurrence and amount of sonoporation, while the opening of cell-cell contacts could not be predicted from microbubble behavior. Microbubble-mediated opening of cell-cell contacts only occurred upon sonoporation and was influenced significantly by the initial cell state. Therefore, our results suggest that opening of cell-cell contacts is a biological response as a consequence of sonoporation, instead of an independent drug delivery pathway. These novel insights will aid the development of safe and efficient microbubble-mediated drug delivery.

Supplementary data to this article can be found online at https://doi.org/10.1016/j.jconrel.2020.03.038.

Acknowledgements

This work was supported by the Applied and Engineering Sciences TTW (Veni-project 13669), part of NWO. The authors would like to thank Phoei Ying Tang from the Department of Biomedical Engineering for assistance during experiments and cell culture and Michiel Manten and Geert Springeling from the Department of Experimental Medical Instrumentation for technical assistance, all from the Erasmus Medical Center, the Netherlands.

References

[1] K. Kooiman, H.J. Vos, M. Versluis, N. de Jong, Acoustic behavior of microbubbles and implications for drug delivery, Adv. Drug Deliv. Rev. 72 (2014) 28–48, https://doi.org/10.1016/j.addr.2014.03.003.
[2] I. Lentacker, I. De Cock, R. Deckers, S.C. De Smedt, C.T.W. Moonen, Understanding ultrasound induced sonoporation: definitions and underlying mechanisms, Adv. Drug Deliv. Rev. 72 (2014) 49–64, https://doi.org/10.1016/j.addr.2013.11.008.
[3] S. Roovers, T. Segers, G. Lajoinie, J. Deprez, M. Versluis, S.C. De Smedt, I. Lentacker, The role of ultrasound-driven microbubble dynamics in drug delivery: from microbubble fundamentals to clinical translation, Langmuir. 35 (2019) 10173–10191, https://doi.org/10.1021/acs.langmuir.8b03779.
[4] B. Helfield, X. Chen, S.C. Watkins, F.S. Villanueva, Biophysical insight into mechanisms of sonoporation, Proc. Natl. Acad. Sci. 113 (2016) 9983–9988, https://doi.org/10.1073/pnas.1606915113.
[5] B.L. Helfield, X. Chen, B. Qin, S.C. Watkins, F.S. Villanueva, Mechanistic insight into Sonoporation with ultrasound-stimulated polymer microbubbles, Ultrasound Med. Biol. 43 (2017) 2678–2689, https://doi.org/10.1016/j.ultrasmedbio.2017.07.017.
[6] A. van Wamel, K. Kooiman, M. Harteveld, M. Emmer, F.J. ten Cate, M. Versluis, N. de Jong, Vibrating microbubbles poking individual cells: drug transfer into cells via sonoporation, J. Control. Release 112 (2006) 149–155, https://doi.org/10.1016/j.jconrel.2006.02.007.
[7] K. Kooiman, M. Foppen-Harteveld, A.F.W. van der Steen, N. de Jong, Sonoporation of endothelial cells by vibrating targeted microbubbles, J. Control. Release 154 (2011) 35–41, https://doi.org/10.1016/j.jconrel.2011.04.008.
[8] Y. Hu, J.M.F. Wan, A.C.H. Yu, Membrane perforation and recovery dynamics in microbubble-mediated sonoporation, Ultrasound Med. Biol. 39 (2013) 2393–2405, https://doi.org/10.1016/j.ultrasmedbio.2013.08.003.
[9] I. De Cock, E. Zagato, K. Braeckmans, Y. Luan, N. de Jong, S.C. De Smedt, I. Lentacker, Ultrasound and microbubble mediated drug delivery: acoustic pressure as determinant for uptake via membrane pores or endocytosis, J. Control. Release 197 (2015) 20–28, https://doi.org/10.1016/j.jconrel.2014.10.031.
[10] S. Roovers, G. Lajoinie, I. De Cock, T. Brans, H. Dewitte, K. Braeckmans, M. Versuis, S.C. De Smedt, I. Lentacker, Sonoprinting of nanoparticle-loaded microbubbles: unraveling the multi-timescale mechanism, Biomaterials. 217 (2019) 119250, https://doi.org/10.1016/j.biomaterials.2019.119250.
[11] I. Lentacker, N. Wang, R.E. Vandenbroucke, J. Demeester, S.C. De Smedt, N.N. Sanders, Ultrasound exposure of Lipoplex loaded microbubbles facilitates direct cytoplasmic entry of the Lipoplexes, Mol. Pharm. 6 (2009) 457–467, https://doi.org/10.1021/mp800154s.
[12] X. Chen, R.S. Leow, Y. Hu, J.M.F. Wan, A.C.H. Yu, Single-site sonoporation disrupts actin cytoskeleton organization, J. R. Soc. Interface 11 (2014) 20140071, https://doi.org/10.1098/rsif.2014.0071.
[13] I. De Cock, G. Lajoinie, M. Versluis, S.C. De Smedt, I. Lentacker, Sonoprinting and the importance of microbubble loading for the ultrasound mediated cellular delivery of nanoparticles, Biomaterials. 83 (2016) 294–307, https://doi.org/10.1016/j.biomaterials.2016.01.022.
[14] M. Emmer, H.J. Vos, M. Versluis, N. de Jong, Radial modulation of single microbubbles, IEEE Trans. Ultrason. Ferroelectr. Freq. Control 56 (2009) 2370–2379, https://doi.org/10.1109/TUFFC.2009.1325.
[15] D. Maresca, M. Emmer, P.L.M.J. van Neer, H.J. Vos, M. Versluis, M. Muller, N. de Jong, A.F.W. van der Steen, Acoustic sizing of an ultrasound contrast agent, Ultrasound Med. Biol. 36 (2010) 1713–1721, https://doi.org/10.1016/j.ultrasmedbio.2010.06.014.
[16] T. van Rooij, I. Skachkov, I. Beekers, K.R. Lattwein, J.D. Voorneveld, T.J.A. Kokhuis, D. Bera, Y. Luan, A.F.W. van der Steen, N. de Jong, K. Kooiman, Viability of endothelial cells after ultrasound-mediated sonoporation: influence of targeting, oscillation, and displacement of microbubbles, J. Control. Release 238 (2016) 197–211, https://doi.org/10.1016/j.jconrel.2016.07.037.
[17] N. Kudo, K. Okada, K. Yamamoto, Sonoporation by single-shot pulsed ultrasound with microbubbles adjacent to cells, Biophys. J. 96 (2009) 4866–4876, https://doi.org/10.1016/j.bpj.2009.02.072.
[18] Z. Fan, H. Liu, M. Mayer, C.X. Deng, Spatiotemporally controlled single cell sonoporation, Proc. Natl. Acad. Sci. 109 (2012) 16486–16491, https://doi.org/10.1073/pnas.1208198109.
[19] Y. Zhou, K. Yang, J. Cui, J.Y. Ye, C.X. Deng, Controlled permeation of cell membrane by single bubble acoustic cavitation, J. Control. Release 157 (2012) 103–111, https://doi.org/10.1016/j.jconrel.2011.09.068.
[20] Z. Fan, D. Chen, C.X. Deng, Improving ultrasound gene transfection efficiency by controlling ultrasound excitation of microbubbles, J. Control. Release 170 (2013) 401–413, https://doi.org/10.1016/j.jconrel.2013.05.039.
[21] K. Hynynen, Ultrasound for drug and gene delivery to the brain, Adv. Drug Deliv. Rev. 60 (2008) 1209–1217, https://doi.org/10.1016/j.addr.2008.03.010.
[22] E.E. Konofagou, Optimization of the ultrasound-induced blood-brain barrier opening, Theranostics. 2 (2012) 1223–1237, https://doi.org/10.7150/thno.5576.
[23] P. Qin, T. Han, A.C.H. Yu, L. Xu, Mechanistic understanding the bioeffects of ultrasound-driven microbubbles to enhance macromolecule delivery, J. Control. Release 272 (2018) 169–181, https://doi.org/10.1016/j.jconrel.2018.01.001.
[24] P.C. Brooks, R.A. Clark, D.A. Cheresh, Requirement of vascular integrin alpha v beta 3 for angiogenesis, Science (80-.) 264 (1994), https://doi.org/10.1126/science.7512751 (569 LP – 571).
[25] F.W. Kremkau, General principles of echocardiography, ASE's Compr. Echocardiogr. 2015, pp. 11–24, , https://doi.org/10.1016/B978-0-323-26011-4.09971-X.
[26] I. Beekers, T. van Rooij, A.F.W. van der Steen, N. de Jong, M.D. Verweij, K. Kooiman, Acoustic characterization of the CLINIcell for ultrasound contrast agent studies, IEEE Trans. Ultrason. Ferroelectr. Freq. Control 66 (2019) 244–246, https://doi.org/10.1109/TUFFC.2018.2881724.
[27] T. van Rooij, Y. Luan, G. Renaud, A.F.W. van der Steen, M. Versluis, N. de Jong, K. Kooiman, Non-linear response and viscoelastic properties of lipid-coated microbubbles: DSPC versus DPPC, Ultrasound Med. Biol. 41 (2015) 1432–1445, https://doi.org/10.1016/j.ultrasmedbio.2015.01.004.
[28] K. Kooiman, T.J.A. Kokhuis, T. van Rooij, I. Skachkov, A. Nigg, J.G. Bosch, A.F.W. van der Steen, W.A. van Cappellen, N. de Jong, DSPC or DPPC as main shell component influences ligand distribution and binding area of lipid-coated targeted microbubbles, Eur. J. Lipid Sci. Technol. 116 (2014) 1217–1227, https://doi.org/10.1002/ejlt.201300434.
[29] A.L. Klibanov, P.T. Rasche, M.S. Hughes, J.K. Wojdyla, K.P. Galen, J.H. Wible, G.H. Brandenburger, Detection of individual microbubbles of ultrasound contrast agents: imaging of free-floating and targeted bubbles, Investig. Radiol. 39 (2004) 187–195, https://doi.org/10.1097/01.rli.0000115926.96796.75.
[30] J.R. Lindner, J. Song, J. Christiansen, A.L. Klibanov, F. Xu, K. Ley, Ultrasound assessment of inflammation and renal tissue injury with microbubbles targeted to P-selectin, Circulation. 104 (2001) 2107–2112, https://doi.org/10.1161/hc4201.097061.
[31] I. Skachkov, Y. Luan, A.F.W. van der Steen, N. de Jong, K. Kooiman, Targeted microbubble mediated sonoporation of endothelial cells in vivo, IEEE Trans. Ultrason. Ferroelectr. Freq. Control 61 (2014) 1661–1667, https://doi.org/10.1109/TUFFC.2014.006440.
[32] P.A. Dayton, D. Pearson, J. Clark, S. Simon, P.A. Schumann, R. Zutshi, T.O. Matsunaga, K.W. Ferrara, Ultrasonic analysis of peptide- and antibody-targeted microbubble contrast agents for molecular imaging of αvβ3-expressing cells, Mol. Imaging 3 (2004) 125–134, https://doi.org/10.1162/1535350041464883.
[33] V. Daeichin, K. Kooiman, I. Skachkov, J.G. Bosch, T.L. Theelen, K. Steiger, A. Needles, B.J. Janssen, M.J.A.P. Daemen, A.F.W. van der Steen, N. de Jong, J.C. Sluimer, Quantification of endothelial αvβ3 expression with high-frequency ultrasound and targeted microbubbles: in vitro and in vivo studies, Ultrasound Med. Biol. 42 (2016) 2283–2293, https://doi.org/10.1016/j.ultrasmedbio.2016.05.005.
[34] D.B. Ellegala, H. Leong-Poi, J.E. Carpenter, A.L. Klibanov, S. Kaul, M.E. Shaffrey,

J. Sklenar, J.R. Lindner, Imaging tumor angiogenesis with contrast ultrasound and microbubbles targeted to αvβ3, Circulation. 108 (2003) 336–341, https://doi.org/10.1161/01.CIR.0000080326.15367.0C.
[35] C.T. Chin, C. Lancée, J. Borsboom, F. Mastik, M.E. Frijlink, N. de Jong, M. Versluis, D. Lohse, Brandaris 128: a digital 25 million frames per second camera with 128 highly sensitive frames, Rev. Sci. Instrum. 74 (2003) 5026–5034, https://doi.org/10.1063/1.1626013.
[36] I. Beekers, K.R. Lattwein, J.J.P. Kouijzer, S.A.G. Langeveld, M. Vegter, R. Beurskens, F. Mastik, R. Verduyn Lunel, E. Verver, A.F.W. van der Steen, N. de Jong, K. Kooiman, Combined confocal microscope and Brandaris 128 ultra-high-speed camera, Ultrasound Med. Biol. 45 (2019) 2575–2582, https://doi.org/10.1016/j.ultrasmedbio.2019.06.004.
[37] M. Edidin, A rapid, quantitative fluorescence assay for cell damage by cytotoxic antibodies, J. Immunol. 104 (1970) 1303–1306 http://www.jimmunol.org/content/104/5/1303.abstract.
[38] M. Wang, Y. Zhang, C. Cai, J. Tu, X. Guo, D. Zhang, Sonoporation-induced cell membrane permeabilization and cytoskeleton disassembly at varied acoustic and microbubble-cell parameters, Sci. Rep. 8 (2018) 3885, https://doi.org/10.1038/s41598-018-22056-8.
[39] E.K. Juang, I. De Cock, C. Keravnou, M.K. Gallagher, S.B. Keller, Y. Zheng, M. Averkiou, Engineered 3D microvascular networks for the study of ultrasound-microbubble-mediated drug delivery, Langmuir. 35 (2019) 10128–10138, https://doi.org/10.1021/acs.langmuir.8b03288.
[40] L. Schermelleh, R. Heintzmann, H. Leonhardt, A guide to super-resolution fluorescence microscopy, J. Cell Biol. 190 (2010) 165–175, https://doi.org/10.1083/jcb.201002018.
[41] S.M. van der Meer, B. Dollet, M.M. Voormolen, C.T. Chin, A. Bouakaz, N. de Jong, M. Versluis, D. Lohse, Microbubble spectroscopy of ultrasound contrast agents, J. Acoust. Soc. Am. 121 (2007) 648–656, https://doi.org/10.1121/1.2390673.
[42] B.L. Helfield, E. Cherin, F.S. Foster, D.E. Goertz, Investigating the subharmonic response of individual phospholipid encapsulated microbubbles at high frequencies: a comparative study of five agents, Ultrasound Med. Biol. 38 (2012) 846–863, https://doi.org/10.1016/j.ultrasmedbio.2012.01.011.
[43] K. Kooiman, T. van Rooij, B. Qin, F. Mastik, H.J. Vos, M. Versluis, A.L. Klibanov, N. de Jong, F.S. Villanueva, X. Chen, Focal areas of increased lipid concentration on the coating of microbubbles during short tone-burst ultrasound insonification, PLoS One 12 (2017) e0180747, , https://doi.org/10.1371/journal.pone.0180747.
[44] T. van Rooij, I. Beekers, K.R. Lattwein, A.F.W. van der Steen, N. de Jong, K. Kooiman, Vibrational responses of bound and nonbound targeted lipid-coated single microbubbles, IEEE Trans. Ultrason. Ferroelectr. Freq. Control 64 (2017) 785–797, https://doi.org/10.1109/TUFFC.2017.2679160.
[45] N. de Jong, M. Emmer, C.T. Chin, A. Bouakaz, F. Mastik, D. Lohse, M. Versluis, "Compression-only" behavior of phospholipid-coated contrast bubbles, Ultrasound Med. Biol. 33 (2007) 653–656, https://doi.org/10.1016/j.ultrasmedbio.2006.09.016.
[46] M. Emmer, A. van Wamel, D.E. Goertz, N. de Jong, The onset of microbubble vibration, Ultrasound Med. Biol. 33 (2007) 941–949, https://doi.org/10.1016/j.ultrasmedbio.2006.11.004.
[47] D. Tsvirkun, A. Grichine, A. Duperray, C. Misbah, L. Bureau, Microvasculature on a chip: study of the endothelial surface layer and the flow structure of red blood cells, Sci. Rep. 7 (2017) 1–11, https://doi.org/10.1038/srep45036.
[48] N. de Jong, M. Emmer, A. van Wamel, M. Versluis, Ultrasonic characterization of ultrasound contrast agents, Med. Biol. Eng. Comput. 47 (2009) 861–873, https://doi.org/10.1007/s11517-009-0497-1.
[49] P. Marmottant, S. van der Meer, M. Emmer, M. Versluis, N. de Jong, S. Hilgenfeldt, D. Lohse, A model for large amplitude oscillations of coated bubbles accounting for buckling and rupture, J. Acoust. Soc. Am. 118 (2005) 3499–3505, https://doi.org/10.1121/1.2109427.
[50] J. Sijl, M. Overvelde, B. Dollet, V. Garbin, N. de Jong, D. Lohse, M. Versluis, "Compression-only" behavior: a second-order nonlinear response of ultrasound contrast agent microbubbles, J. Acoust. Soc. Am. 129 (2011) 1729–1739, https://doi.org/10.1121/1.3505116.
[51] H. Maeda, Macromolecular therapeutics in cancer treatment: the EPR effect and beyond, J. Control. Release 164 (2012) 138–144, https://doi.org/10.1016/j.jconrel.2012.04.038.
[52] H. Hashizume, P. Baluk, S. Morikawa, J.W. McLean, G. Thurston, S. Roberge, R.K. Jain, D.M. McDonald, Openings between defective endothelial cells explain tumor vessel leakiness, Am. J. Pathol. 156 (2000) 1363–1380, https://doi.org/10.1016/S0002-9440(10)65006-7.
[53] G.P. van Nieuw Amerongen, V.W.M. van Hinsbergh, Targets for pharmacological intervention of endothelial hyperpermeability and barrier function, Vasc. Pharmacol. 39 (2002) 257–272, https://doi.org/10.1016/S1537-1891(03)00014-4.
[54] D.M. McDonald, G. Thurston, P. Baluk, Endothelial gaps as sites for plasma leakage in inflammation, Microcirculation. 6 (1999) 7–22, https://doi.org/10.1111/j.1549-8719.1999.tb00084.x.
[55] R.E. Kumon, M. Aehle, D. Sabens, P. Parikh, Y.W. Han, D. Kourennyi, C.X. Deng, Spatiotemporal effects of Sonoporation measured by real-time calcium imaging, Ultrasound Med. Biol. 35 (2009) 494–506, https://doi.org/10.1016/j.ultrasmedbio.2008.09.003.
[56] N. Lipsman, Y. Meng, A.J. Bethune, Y. Huang, B. Lam, M. Masellis, N. Herrmann, C. Heyn, I. Aubert, A. Boutet, G.S. Smith, K. Hynynen, S.E. Black, Blood–brain barrier opening in Alzheimer's disease using MR-guided focused ultrasound, Nat. Commun. 9 (2018) 2336, https://doi.org/10.1038/s41467-018-04529-6.
[57] T. Mainprize, N. Lipsman, Y. Huang, Y. Meng, A. Bethune, S. Ironside, C. Heyn, R. Alkins, M. Trudeau, A. Sahgal, J. Perry, K. Hynynen, Blood-brain barrier opening in primary brain tumors with non-invasive MR-guided focused ultrasound: a clinical safety and feasibility study, Sci. Rep. 9 (2019) 321, https://doi.org/10.1038/s41598-018-36340-0.